

# **Four-Point Bending Testing of 8-in. (200-mm) Diameter AWWA C900 DR14 iPVC Pipe**

**Shih-Hung Chiu**

**Shakhzod Takhirov**

**Kenichi Soga**



**Berkeley**  
**CENTER FOR**  
**Smart Infrastructure**

CSI Report 2023/03  
Center for Smart Infrastructure (CSI)  
Department of Civil and Environmental Engineering  
University of California, Berkeley May 2023

## EXECUTIVE SUMMARY

This report describes the experimental results of the performance of 8 inches AWWA C900 DR14 iPVC pipe under bending force. The pipe is corrosive resistant and is known to be capable of tolerating large deformations to improve seismic resiliency. Two types of restraints for connecting the pipes were adopted in the experiments. The lab tests were conducted under a monotonic force applied at the center of the specimens perpendicular to the pipeline direction. It was tested up to severe pipe damage or significant water leakage. Distributed fiber optic sensors were adopted to capture the pipeline behavior and to get insight into the deformation and failure mechanism. The failure modes regarding different restraints are discussed herein.

**Keywords:** *iPVC pipe, water pipelines, fiber optic, leakage, sensors.*

## **ACKNOWLEDGMENTS**

The funding for this project was provided by the East Bay Municipal Utility District (EBMUD). The completion of the work would not be possible without the support of Llyr Griffith, John Kochan, Irik Larson, and Phillip Wong of the University of California, Berkeley. Active involvement and guidance from David Katzev of EBMUD are greatly appreciated.

## **DISCLAIMER**

Any opinions, findings, conclusions, or recommendations expressed in this material are those of the author(s) and do not necessarily reflect those of the University of California, Berkeley.

# CONTENTS

<b>EXECUTIVE SUMMARY</b> .....	<b>II</b>
<b>ACKNOWLEDGMENTS</b> .....	<b>III</b>
<b>DISCLAIMER</b> .....	<b>IV</b>
<b>CONTENTS</b> .....	<b>V</b>
<b>LIST OF FIGURES</b> .....	<b>VI</b>
<b>LIST OF TABLES</b> .....	<b>VII</b>
<b>1 Introduction</b> .....	<b>8</b>
<b>2 Experimental Setup</b> .....	<b>9</b>
<b>3 Instrumentation</b> .....	<b>10</b>
<b>3.1 Wire Pots</b> .....	<b>10</b>
<b>3.2 Fiber Optic Sensors</b> .....	<b>11</b>
<b>4 Test Results</b> .....	<b>13</b>
<b>4.1 Calculation Approach</b> .....	<b>13</b>
<b>4.2 Experimental Data Analysis</b> .....	<b>13</b>
4.2.1 Moment and Rotation .....	13
4.2.2 Large Deformation and Failure Modes.....	14
4.2.3 Axial Strains .....	16
4.2.4 Hoop Strains .....	21
<b>5 Conclusions</b> .....	<b>26</b>
<b>6 References</b> .....	<b>27</b>
<b>Appendix A: Additional Specimen with RCT Restraint Test Result</b> .....	<b>28</b>
<b>Appendix B: Distributed Fiber Optic Sensing</b> .....	<b>30</b>
<b>Appendix C: Fiber Optic Sensors Result</b> .....	<b>32</b>

## LIST OF FIGURES

Figure 1-1 Schematic of the bell of AWWA C900 DR14 iPVC pipe (PPI, n.d.).....	8
Figure 1-2 Restraints for the specimens.....	8
Figure 2-1 Specimen 1 (EBAA 1900 restraint) experimental setup.....	9
Figure 2-2 Specimen 2 (RCT restraint) experimental setup.....	9
Figure 3-1 Instrumentation plan of Specimen 1 (EBAA 1900 restraint).....	10
Figure 3-2 Instrumentation plan of Specimen 2 (RCT restraint).....	11
Figure 3-3 Instrumentation plan of fiber optic sensors of Specimen 1 (EBAA 1900 restraint).....	12
Figure 3-4 Instrumentation plan of fiber optic sensors of Specimen 2 (RCT restraint).....	12
Figure 4-1 Moment, rotation, and water pressure of the tests. (a) Joint rotation versus moment (b) Joint rotation versus water pressure.....	14
Figure 4-2 Large deformation of Specimen 1 and 2.....	15
Figure 4-3 Failure of Specimen 2.....	15
Figure 4-4 Axial strain vs joint rotation (a) West pipe of Specimen 1, (b) East pipe of Specimen 1, (c) West pipe of Specimen 2, (d) East pipe of Specimen 2.....	17
Figure 4-5 Axial strain development of west pipe of Specimen 1 under 18-degree rotation condition. (a) South side, (b) Top side, (c) North side, (d) Bottom side.....	18
Figure 4-6 Axial strain development of east pipe of Specimen 1 under 18-degree rotation condition. (a) South side, (b) Top side, (c) North side, (d) Bottom side.....	19
Figure 4-7 Axial strain development of west pipe of Specimen 2 under 18-degree rotation condition. (a) South side, (b) Top side, (c) North side, (d) Bottom side.....	20
Figure 4-8 Axial strain development of east pipe of Specimen 2 under 18-degree rotation condition. (a) South side, (b) Top side, (c) North side, (d) Bottom side.....	21
Figure 4-9 Strain distribution in the circumferential direction of Specimen 1 under 18-degree rotation condition. (a) sensor on the west pipe (b) sensor on the bell to the west of the center (c) sensor on the bell to the east of the center (d) sensor on the east pipe.....	22
Figure 4-10 Sketch of pipe cross-section deformation mechanism under bending condition.....	23
Figure 4-11 Sketch of EBAA 1900 restraint deformation mechanism.....	23
Figure 4-12 Strain distribution in the circumferential direction of Specimen 2 under 18-degree rotation condition. (a) sensor on the west pipe (b) sensor on the bell to the west of the center (c) sensor on the bell to the east of the center (d) sensor on the east pipe.....	25
Figure 4-13 Sketch of strain concentration on pipes of Specimen 2.....	25

## LIST OF TABLES

Table 2-1 Test log .....	10
Table 3-1 Conventional instrumentation for AWWA C900 iPVC 4-point bending test .....	11
Table 3-2 Fiber optic sensors for AWWA C900 iPVC 4-point bending test .....	12
Table 4-1 Summary of the tests .....	15

# 1 Introduction

This report summarizes the experimental results of two 4-point bending tests performed on 8-inch AWWA C900 DR14 iPVC pipes. The pipe is corrosive resistant and is known to be capable of tolerating large deformations which could improve the seismic resiliency of pipeline systems.

The pipe is equipped with a bell used for connecting the pipes. The pipe is designed to be inserted into the bell pass through a rubber gasket, which is deployed for water leaking prevention purposes, as shown in Figure 1-1. Two types of restraints were used for the experiments, EBAA 1900 restraint and RCT restraint, as shown in Figure 1-2. The restraints are used to restrict the relative movement between the pipes. Both the EBAA 1900 and RCT restraints are made of ductile iron. However, their locking mechanism is different. For EBAA 1900, four rods are used to prevent the pipes from moving apart. Two bolts are deployed to the serrated rings to provide nominal forces for the friction between the pipe and the rings. Instead of having an external locking mechanism, the RCT restraint provides specially designed teeth inside the restraint, which allows only one direction movement (i.e., the direction point into the restraint). In this study, the pipe's bell section was cut to implement the RCT restraint. That is, two identical pipes were connected using the RCT restraint. In addition, rubber gaskets were placed inside the restraint to prevent the water from leaking. This study aims to understand the deflection contraction capacity and failure mechanism of the pipes equipped with the two different restraints under bending force.

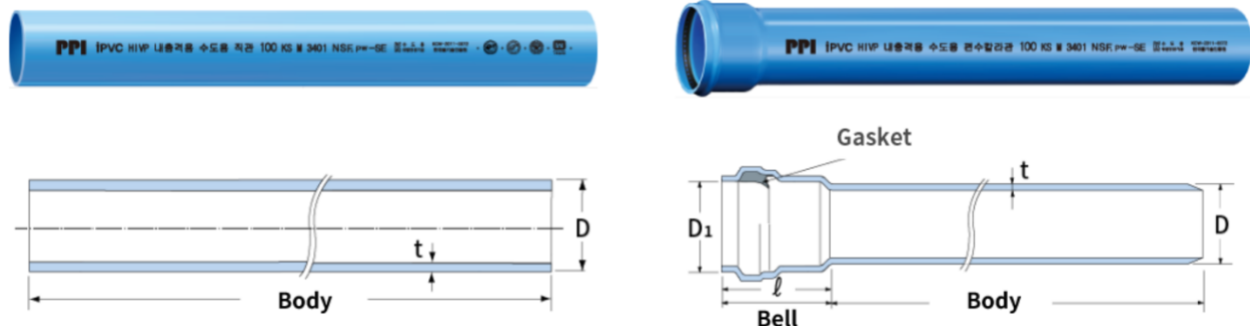
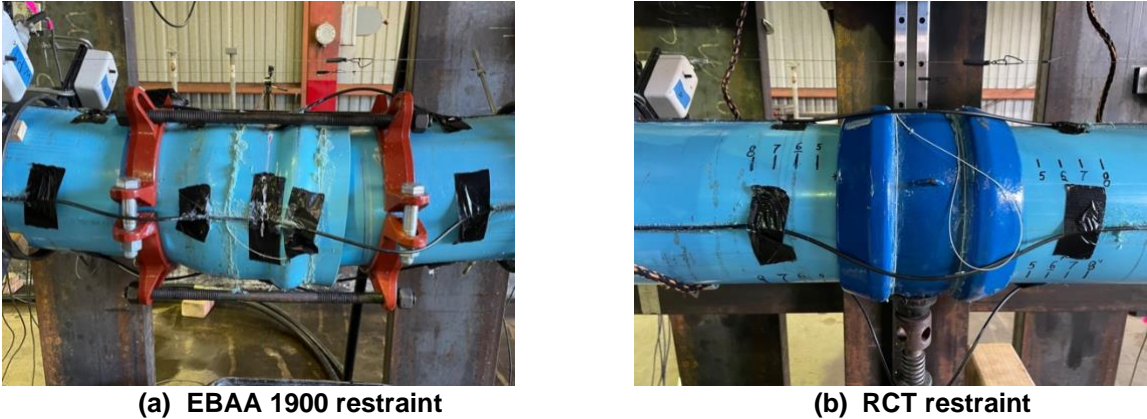


Figure 1-1 Schematic of the bell of AWWA C900 DR14 iPVC pipe (PPI, n.d.)



(a) EBAA 1900 restraint

(b) RCT restraint

Figure 1-2 Restraints for the specimens



Distributed fiber optic sensors were deployed to measure the continuous strain development along the longitudinal and circumferential directions. Wire pots were used for measuring the movement of the specimens. The failure mode and mechanism are discussed in the following sections using the experimental data.

## 2 Experimental Setup

The experimental setup was developed at the Center for Smart Infrastructure (CSI) of UC Berkeley. The overview of the fully assembled setups of the 4-point bending tests is shown in Figure 2-1 and Figure 2-2. Specimen 1 was equipped with EBAA 1900 restraint, whereas Specimen 2 were equipped with RCT restraint. A self-react frame was designed to accommodate the loading and reaction sections. A 20-kip pulling and 25-kip pushing capacity with 40 inches total stroke hydraulic actuator was adopted in the experiments. The actuator was located at the center of the specimens, defined as 4.5 inches away from the bell face for Specimen 1 and the mid-point of RCT restraint for Specimen 2. A steel spreader beam was located beneath the actuator used for load transfer purposes. The force was first applied to the beam and transferred to two saddles on the pipes 30 inches from the center. The roller supports were located 75 inches away from the center on both ends of the specimens. The specimens were pressurized to 70 psi one day before the experiment. The test log is presented in Table 2-1.



Figure 2-1 Specimen 1 (EBAA 1900 restraint) experimental setup



Figure 2-2 Specimen 2 (RCT restraint) experimental setup

**Table 2-1 Test log**

Test No	Specimen	Test date	Restraint
1	Specimen 1	10/14/2022	EBAA 1900
2	Specimen 2	11/10/2022	RCT

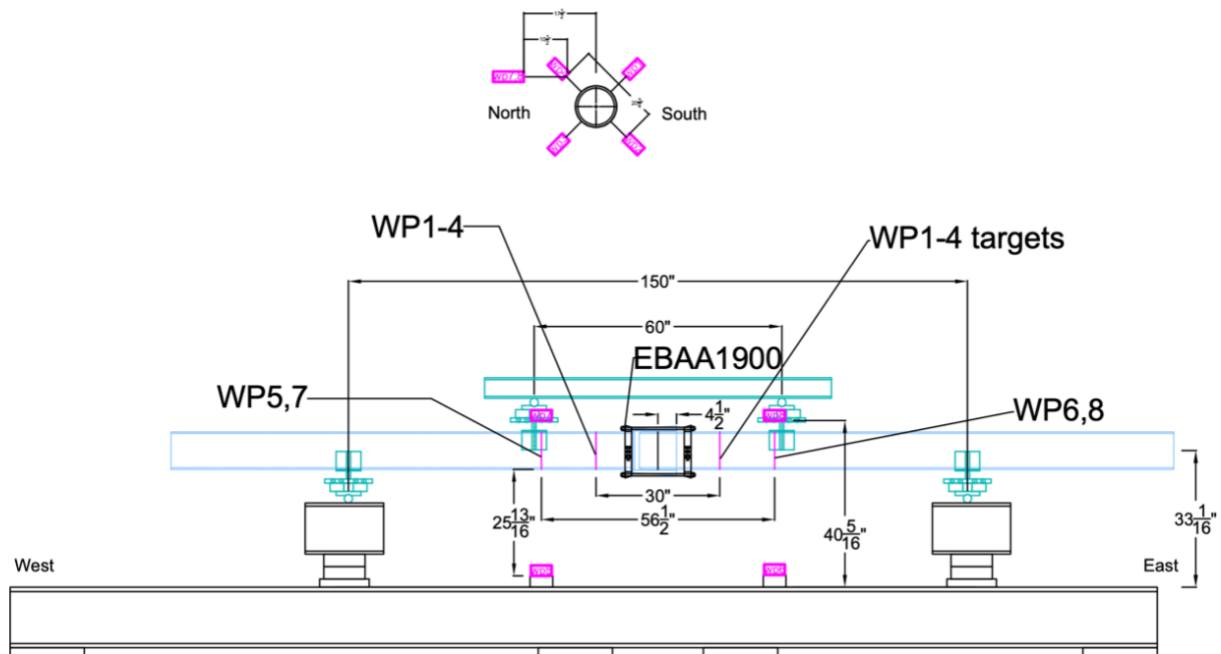
Note that in addition to the two tests, an additional trial test on the specimen equipped with RCT restraint was conducted and the result is reported in Appendix A.

### 3 Instrumentation

The instrumentation consisted of wire pots and distributed fiber optic sensors (DFOS). The instrumentation plan is discussed in the following sections.

#### 3.1 Wire Pots

Eight string pots were installed on the specimens to measure the displacements. Four wire pots were used to measure the joint opening, located 45 degrees apart from the quarter points. Another four wire pots were used for monitoring displacements of the pipes during the experiment. The exact locations of the instruments for the three specimens are shown in Figure 3-1 and Figure 3-2. They were mounted on both ends of the pipes, on the north and bottom sides. The two wire pots mounted on the north side aimed to measure the horizontal displacement, and the ones on the bottom side were attached to monitor the vertical displacements. The local instrument names are shown in Table 3-1.



**Figure 3-1 Instrumentation plan of Specimen 1 (EBAA 1900 restraint)**

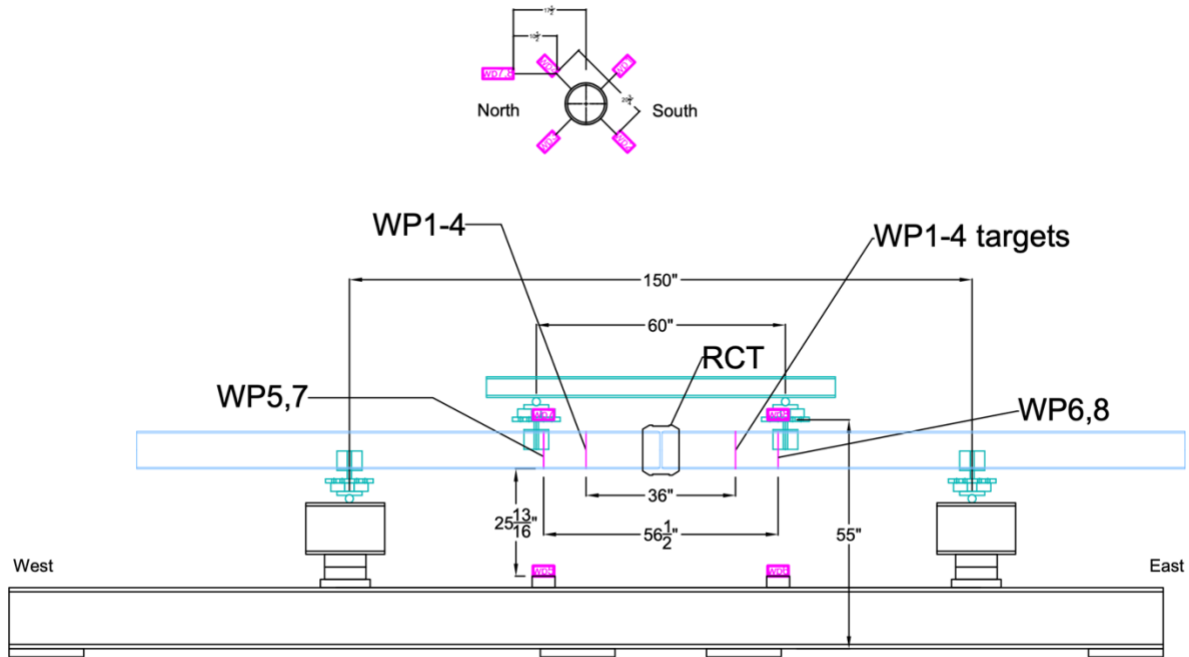


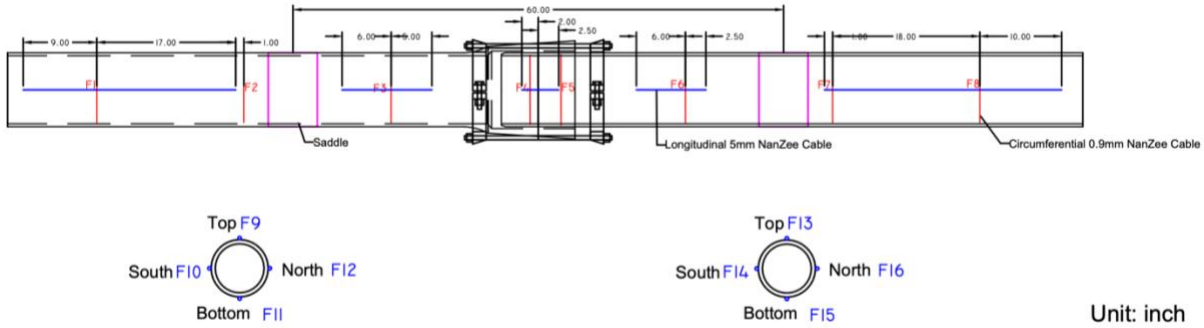
Figure 3-2 Instrumentation plan of Specimen 2 (RCT restraint)

Table 3-1 Conventional instrumentation for AWWA C900 iPVC 4-point bending test

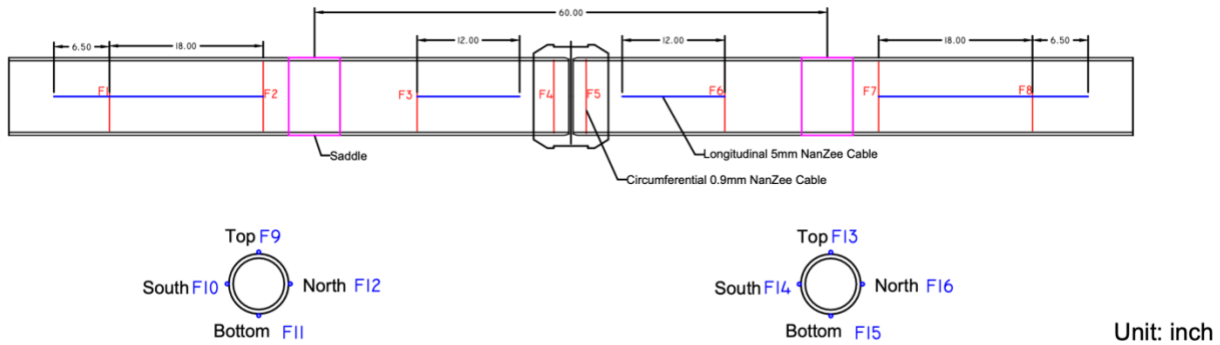
Instrument	Location	Local Instrument Name
Wire Pot	Parallel to Axial Direction, West of Center, Top-south	wp1
	Parallel to Axial Direction, West of Center, South-bottom	wp2
	Parallel to Axial Direction, West of Center, Bottom-north	wp3
	Parallel to Axial Direction, West of Center, North-top	wp4
	Perpendicular to Axial Direction, West of Center, North	wp7
	Perpendicular to Axial Direction, West of Center, Bottom	wp5
	Perpendicular to Axial Direction, East of Center, North	wp8
	Perpendicular to Axial Direction, East of Center, Bottom	wp6

### 3.2 Fiber Optic Sensors

Two types of fiber optic cables manufactured by NanZee Sensing Technology Co. were used; (a) 5 mm diameter armored cable (NanZee 5mm) and (b) 0.9 mm diameter cable (NanZee 0.9mm). 3M SCOTCH-WELD DP8010 epoxy was used to attach the cables to the pipes. Figure 3-3 and Figure 3-4 show the layout and locations of the sensors. NanZee 5mm cables (blue lines) were used in the longitudinal direction to mimic the use on construction sites. They were attached on both pipes, 90 degrees apart, numbered F9-F16. On the other hand, to better understand the deformation mechanism of the pipes, NanZee 0.9mm (red lines) was used for measuring circumferential strains, numbered F1-F9. Three circumferential sensors with about 18-inch spacing were installed on both pipes. In addition, two sensors measured hoop strains were attached at the bell section on Specimen 1, and two circumferential sensors were attached to the RCT restraint for Specimen 2. The local names of DFOS are listed in Table 3-2.



**Figure 3-3 Instrumentation plan of fiber optic sensors of Specimen 1 (EBAA 1900 restraint)**



**Figure 3-4 Instrumentation plan of fiber optic sensors of Specimen 2 (RCT restraint)**

**Table 3-2 Fiber optic sensors for AWWA C900 iPVC 4-point bending test**

Instrument	Location	Local Instrument Name
DFOS	54 inch west of center, Circumferential	F1
	36 inch west of center, Circumferential	F2
	18 inch west of center, Circumferential	F3
	2.5 inch west of center, Circumferential	F4
	2.5 inch east of center, Circumferential	F5
	18 inch east of center, Circumferential	F6
	36 inch east of center, Circumferential	F7
	54 inch east of center, Circumferential	F8
	West pipe, Top, Longitudinal	F9
	West pipe, South, Longitudinal	F10
	West pipe, Bottom, Longitudinal	F11
	West pipe, North, Longitudinal	F12
	East pipe, Top, Longitudinal	F13
	East pipe, South, Longitudinal	F14
	East pipe, Bottom, Longitudinal	F15
	East pipe, North, Longitudinal	F16

A Rayleigh-based optical frequency domain reflectometry (OFDR), Luna ODiSI 6100 series, was used in the experiments for data acquisition. The analyzer is capable of measuring up to 50m long fiber optic cable with an accuracy of less than  $\pm 1$  micro strain when taking a measurement every 0.65mm. Appendix B provides more information about the cables and the analyzer.

## 4 Test Results

All test results are discussed in this section. In addition, a summary of the failure mode and performance of the 8 inches AWWA C900 DR14 iPVC pipe is included.

### 4.1 Calculation Approach

The approaches to calculating the rotation and moment are discussed herein. The pipes are assumed to be rigid bodies, and the rotations of the pipes are computed using equations (1) – (3). The vertical displacements of the pipes were measured by the vertical wire pots (VWP) located beneath the pipes.  $\theta_{west}$  and  $\theta_{east}$  are the rotations of the west pipe and the east pipe, respectively. The overall rotation,  $\theta_{Total}$ , of the joint is defined as the sum of the two side angles.

$$\theta_{west} = \tan^{-1}\left(\frac{\text{vertical displacement of west pipe}}{\text{distance between VWP and the end support}}\right) \quad (1)$$

$$\theta_{east} = \tan^{-1}\left(\frac{\text{vertical displacement of east pipe}}{\text{distance between VWP and the end support}}\right) \quad (2)$$

$$\theta_{Total} = \theta_{west} + \theta_{east} \quad (3)$$

The system is considered to be a simple-supported beam. The self-weight, including the pipe's and water's weight, is assumed to be evenly distributed, and hence the moment introduced by self-weight is calculated based on equation (4), where  $w$  is the uniform load due to the self-weight, and  $l$  is the length of the pipe. The additional moment applied to the central portion of the pipe is calculated using equation (5), where  $P$  is the actuator load, and  $L$  is the distance between the support and the loading location.

$$M_{distrib} = \frac{wl^2}{8} \quad (4)$$

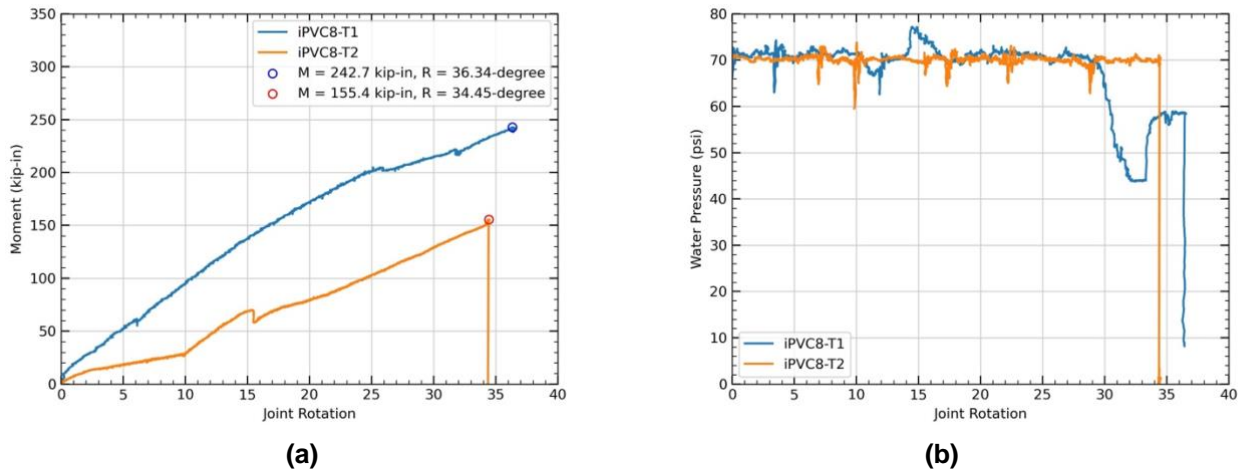
$$M_{central} = \frac{PL}{2} \quad (5)$$

### 4.2 Experimental Data Analysis

#### 4.2.1 Moment and Rotation

The pipes were filled with water and pressurized to 70 psi. A monotonic force perpendicular to the longitudinal axis of the pipeline was applied at the center point of the load transfer beam. Then, the force was transferred to the pipes via the two loading saddles. The moments and rotations of each specimen were calculated using the formulas mentioned above, and the results were visualized in Figure 4-1(a). The maximum rotations with corresponding moments of each specimen are 1) 36.34 degrees rotation with 242.7 kip-in moments, and 2) 34.45 degrees rotation with 155.4 kip-in moments. Specimen 1 showed a large rotation with no pipe failure;

however, Specimen 3 was able to reach a severe pipe failure. For a given rotation, the moment of Specimen 1 was greater than that of Specimen 2, meaning that restraints have a great influence on the moment generated on the pipes. The reason might be because of the length of the restraints. The length of the EBAA 1900 restraint is longer than that of the RCT restraint, resulting in a larger resistant force within the restrained areas and hence acquiring a larger moment to reach a given rotation. In addition, the pipes might be slipping inside the RCT joint and hence resulting in smaller moments. This issue will be investigated in the FE analysis of the experiments planned in the future.



**Figure 4-1 Moment, rotation, and water pressure of the tests. (a) Joint rotation versus moment (b) Joint rotation versus water pressure**

Figure 4-1 (b) shows the relation between water pressure and the joint rotation of each test. For Specimen 1, continuous small leakage of water was observed when the pipes reached about 28-degree rotation. No obvious pipe failure was found throughout the test. A severe water leakage and pipe failure were found in Specimen 2 when the rotation reached 34.45 degrees.

#### 4.2.2 Large Deformation and Failure Modes

No significant failures were found in Specimens 1. Figure 4-2 shows the figures of the two specimens with large deformation. The main difference between these two specimens is the restraints. For Specimen 1, EBAA 1900 restraint, which prevents the pipes from moving apart by the external locking ring, was used. This locking mechanism allowed the pipes to have relative movement within the bell section. While being bent, the top side of the spigot tended to move inward to the bell; on the contrary, the bottom side of the spigot tended to move out from the bell. Because the bottom side of the spigot was moving out, a continuous small leakage can be observed after the specimen reached about 28-degree rotation.

For Specimen 2, RCT restraint, which provides an internal locking mechanism to prevent the pipes from moving apart, was adopted. In this case, pipes were not allowed to move out from the connection section. Hence, no water leakage was found throughout the test before a significant pipe failure. In addition, since the length of the RCT restraint was shorter than the EBAA 1900 restraint, a larger concentrated compressive stress was expected at the boundary of the RCT restraint and the pipes.



**Figure 4-2 Large deformation of Specimen 1 and 2**

A significant pipe failure occurred at the boundary of the RCT restraint and the west-side pipe when the rotation reached about 34.45 degrees, as shown in Figure 4-3. This indicates that the weak point is the edge of the two components. While the pipe was being pushed down, the pipes were squashing, but the restraint was not. This is because the RCT restraint was made of ductile iron which is much stiffer. In addition, because of the stiffness difference at the boundary of the restraint and the pipe, a shear force was developed at the edge resulting in a larger compression force on the top side (12 o'clock), where the pipe first broke.



**Figure 4-3 Failure of Specimen 2**

In addition, for a given rotation, the moments of the specimens with RCT restraint was generally smaller than that of the specimen with EBAA 1900 restraint. This might be because of the shorter length of the restraint and the slipping of the pipes inside the restraint. The results of the tests are summarized in Table 4-1.

**Table 4-1 Summary of the tests**

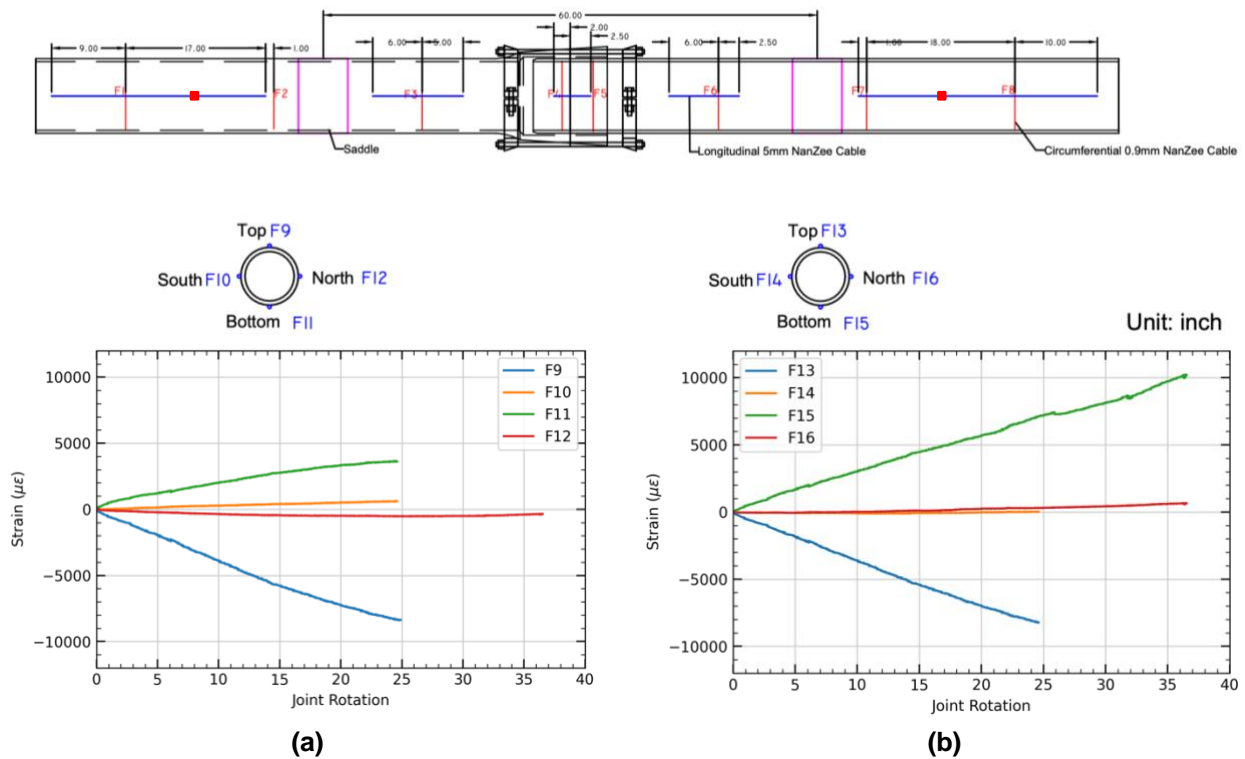
	<b>Max. Moment (kip-in)</b>	<b>Max. Total Rotation (degree)</b>	<b>Pipe Failure</b>	<b>Restraint Type</b>
<b>Specimen 1</b>	242.7	36.34	No	EBAA1900
<b>Specimen 2</b>	155.4	34.45	Yes	RCT

### 4.2.3 Axial Strains

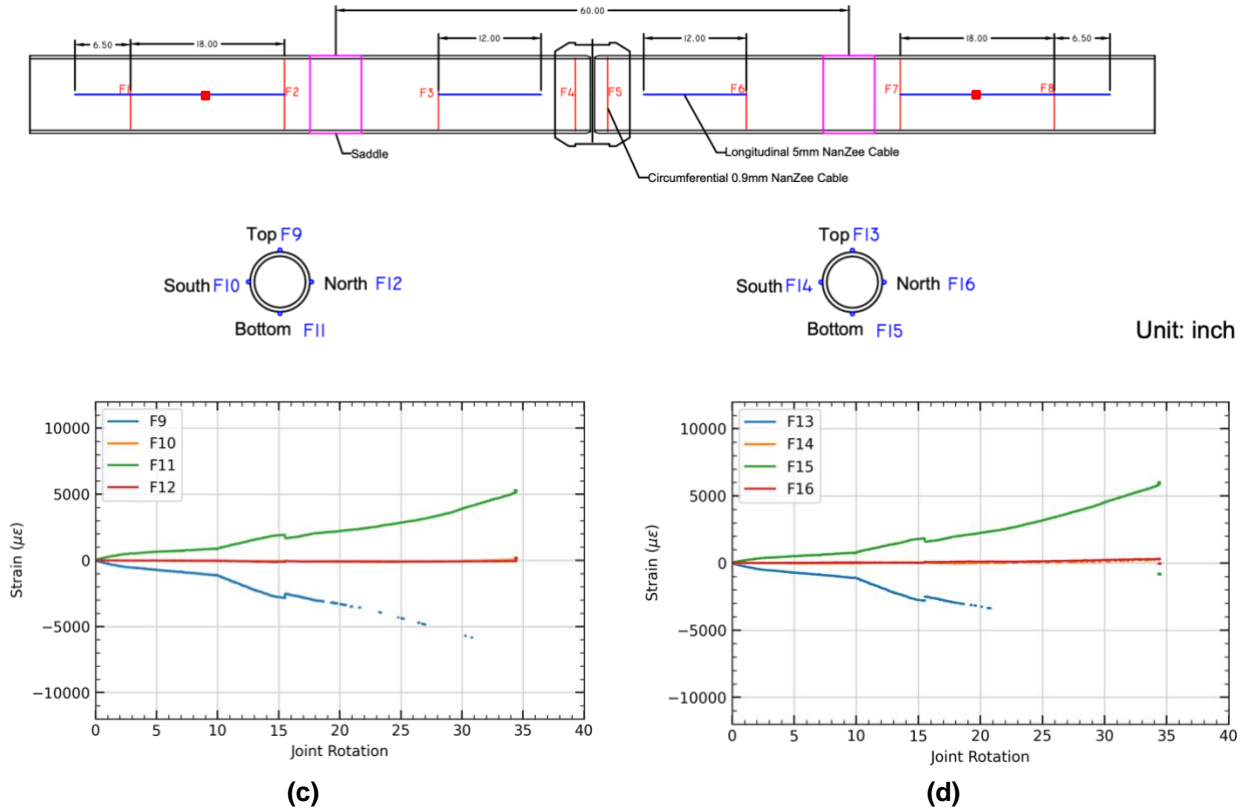
The axial strain results of Specimens 1 and 2 from the distributed fiber optic strain (DFOS) sensors are shown in Figure 4-4 to Figure 4-8.

Although the maximum rotations of the specimens are greater than 30 degrees, some of the sensors did not capture the results when the specimens reached a certain rotation. That is, due to the large deformations, strains of some parts of the specimen were larger than the measuring capacity of DFOS. After reaching about 18 degrees of rotation, some sensors lost their signal. Even though the sensors did not capture the strains of the later stages of the experiment, the DFOS results provide a good insight into how the strains were developing during loading and their deforming mechanism.

Figure 4-4 shows the relationship between the axial strain and joint rotation at the midpoints of F1 and F2 (west pipe), and the midpoints of F7 and F8 (east pipe), measured by the longitudinal sensors. The results from both of the specimens show that the top side of the pipes were under compression and the bottom sides were under tension while being bent. The strains developed on the sides (i.e., north and south) were small and close to zero, meaning that the pipes were squashing eccentrically.



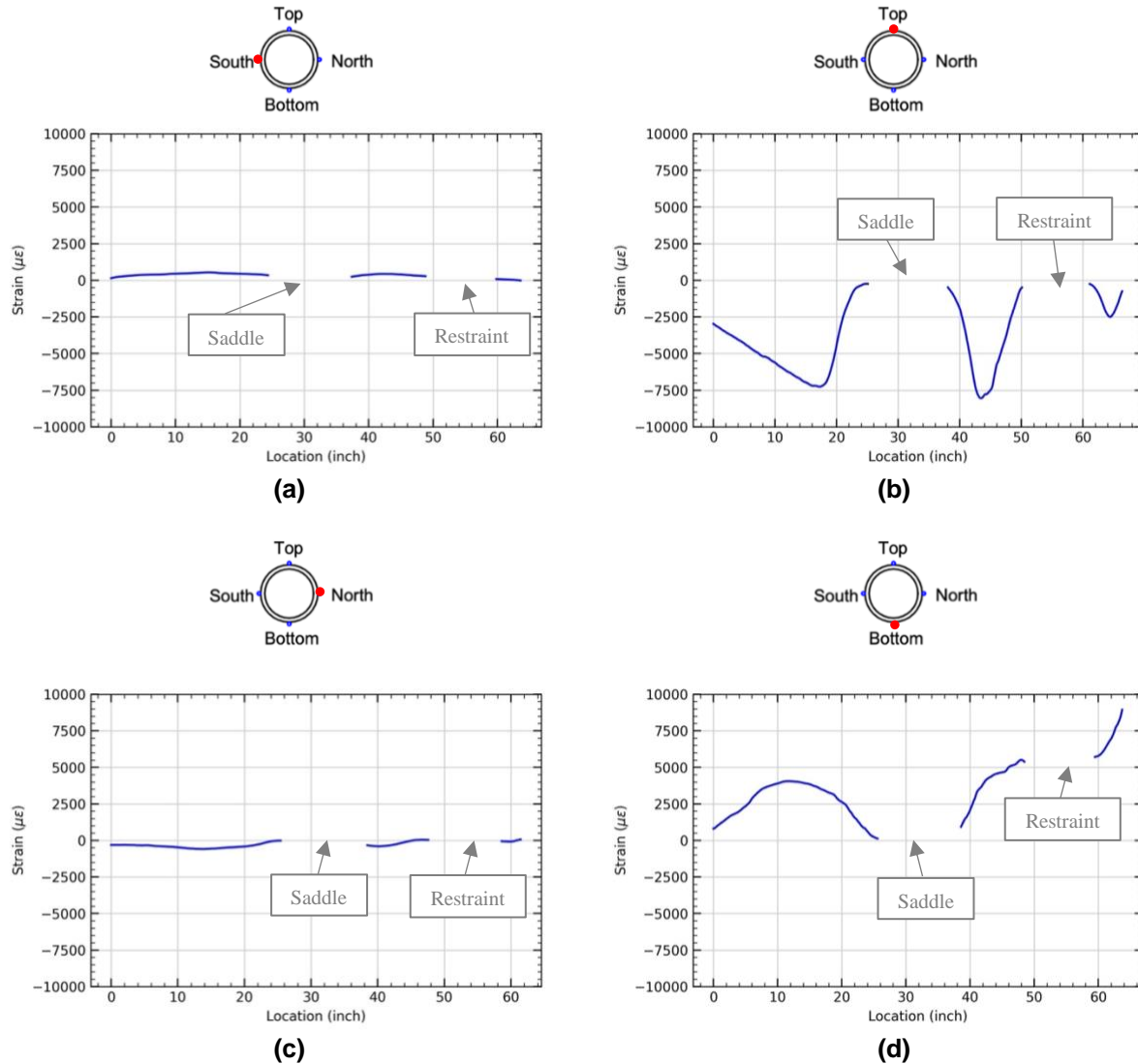




**Figure 4-4 Axial strain vs joint rotation (a) West pipe of Specimen 1, (b) East pipe of Specimen 1, (c) West pipe of Specimen 2, (d) East pipe of Specimen 2**

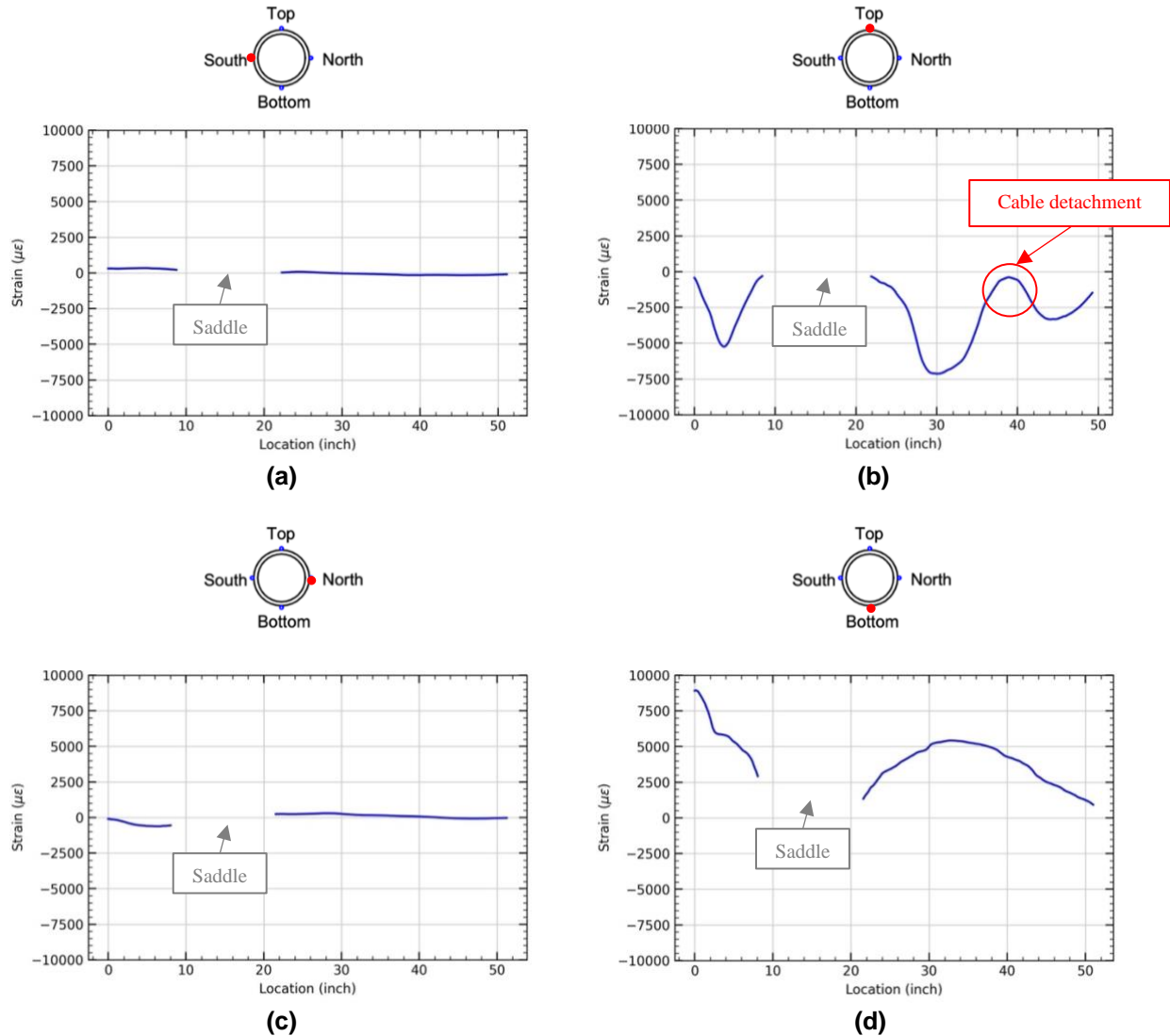
Comparing the magnitude of the strains on the top and bottom sides of the pipes, one can observe that Specimen 1 generally has a larger magnitude than Specimen 2. This is due to the locking mechanism difference. The EBAA 1900 restraint used in Specimen 1 allowed the bell pipe and the spigot to bear against each other, resulting in a larger deformation on the pipes. No failure was found in Specimen 1 until it reached the testing setup's limitation. On the other hand, the material of the RCT restraint used for Specimens 2 was made of ductile iron with much superior stiffness, which resulted in a large strain concentration on the top of the pipes close to the boundary of the restraint but smaller deformation on the rest of the pipes. This localized stress/strain concentration led to failure at the connection boundary in Specimens 2 (see Figure 4-3). The details of the pipe squashing mechanism will be discussed in the following section.

Figure 4-5 shows the axial strain distribution of the west-side of Specimen 1 in Test 1. The figures are plotted from the west to the central location, and the two gaps on the plots are the locations of the loading saddle and the ring of the EBAA 1900 restraint. Clear patterns can be observed; the top side (12 o'clock) was under compression, the bottom side (6 o'clock) was under tension, and the strains on the sides (3 and 9 o'clock) were close to zero, matching the bending theorem. The results measured on the bell (i.e., the right-most section on the figures) show a smaller compressive strain on the top and a larger tensile strain on the bottom. This might be why the pipe within the restraint tended to move out; however, the restraint restricted the movement, resulting in larger tensile stress close to the bell section.



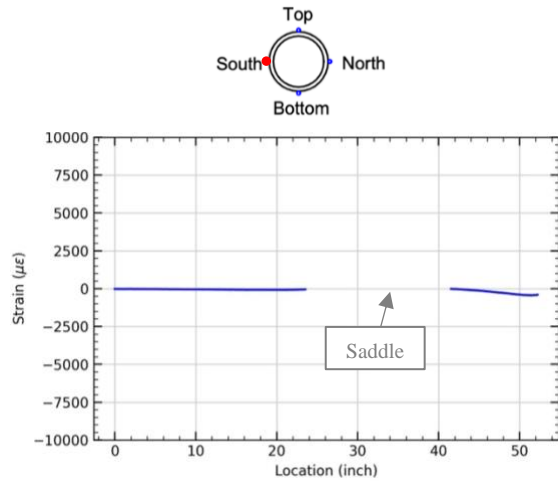
**Figure 4-5 Axial strain development of west pipe of Specimen 1 under 18-degree rotation condition. (a) South side, (b) Top side, (c) North side, (d) Bottom side**

The axial strain distribution results of the east-side of Specimen 1 are similar to the observation from the west-side pipe, as shown in Figure 4-6. Tensile strains developed on the bottom side (6 o'clock), compressive strains were observed on the top side (12 o'clock), and small strains were shown on the sides (3 and 9 o'clock). The smaller compressive strain on the top (12 o'clock) and larger tensile strain on the bottom were found. As mentioned above, this might be because of the restraint restricting the pipes from moving and resulting in tensile stress near the bell section. The smaller values showing on the top side (12 o'clock) close to the 38-inch location, as shown in Figure 4-6(b), were due to cable detachment.

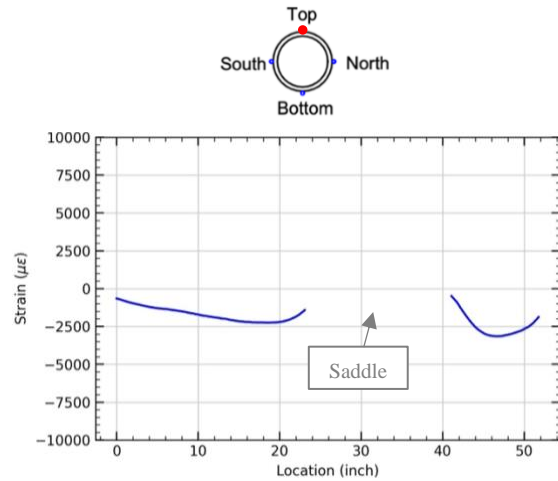


**Figure 4-6 Axial strain development of east pipe of Specimen 1 under 18-degree rotation condition. (a) South side, (b) Top side, (c) North side, (d) Bottom side**

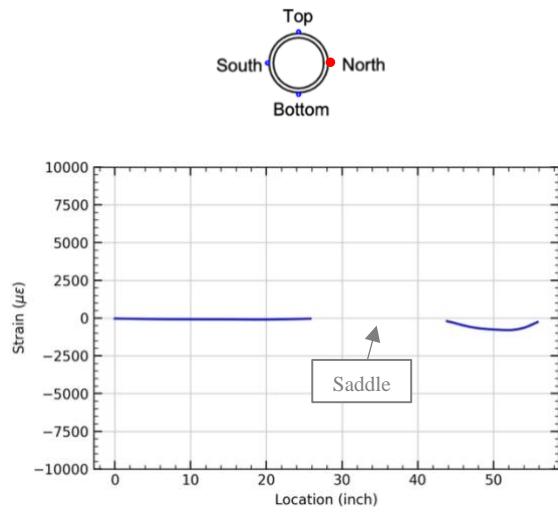
The axial strain results of the west-side of Specimen 2 are shown in Figure 4-7. The results are similar to that of Specimen 1. Tensile strains were observed on the bottom side (6 o'clock), compressive strain on the top side (12 o'clock), and a small strain on the sides (3 and 9 o'clock). Larger compressive strains can be found on the north, south, and top sides (3, 9, and 12 o'clock) close to the restraint. Since the RCT restraint is made of ductile iron, which is much stiffer than the pipe, the restraint did not deform but introduced a shear force close to the boundary of the pipe and the restraint, especially on the top side. Due to Poisson's effect, larger compressive strains were observed on the sides (3 and 9 o'clock) and top side (12 o'clock). A similar phenomenon can be found on the east-side pipe, as shown in Figure 4-8.



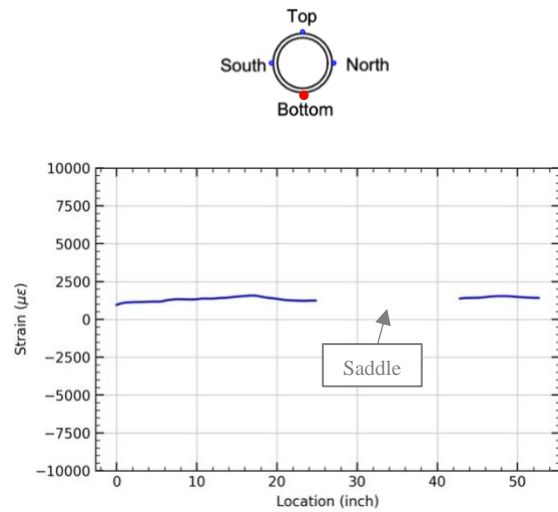
(a)



(b)

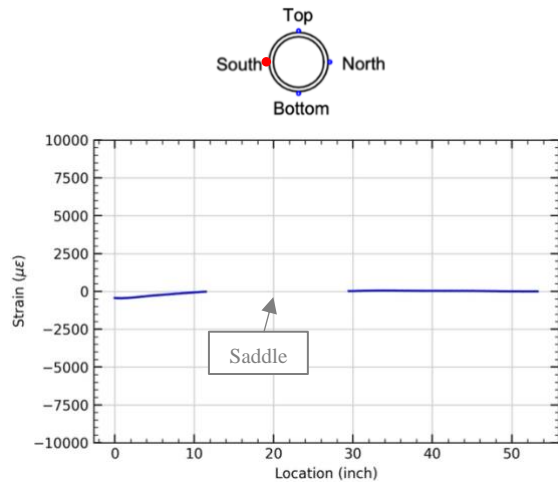


(c)

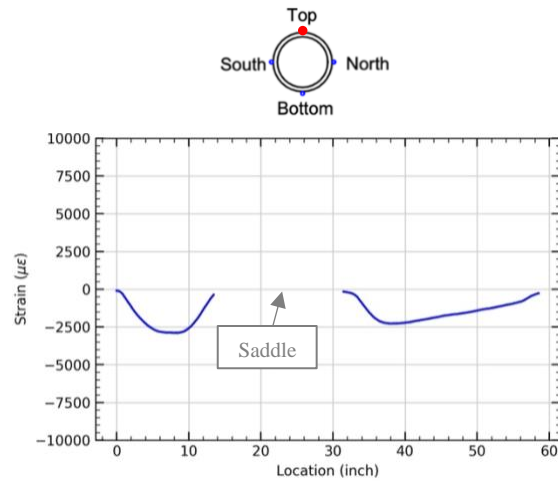


(d)

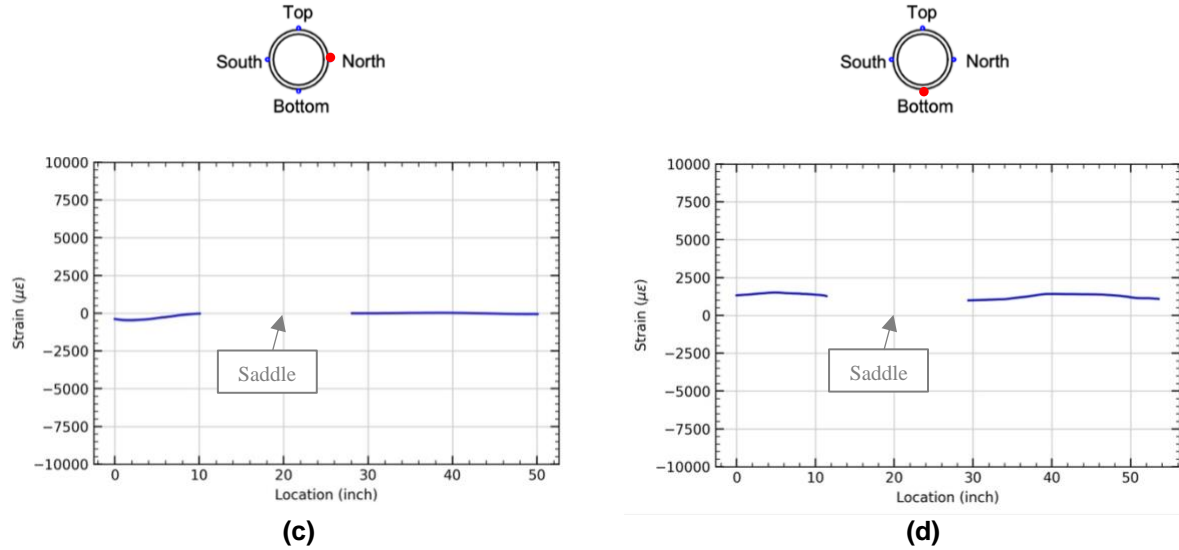
**Figure 4-7 Axial strain development of west pipe of Specimen 2 under 18-degree rotation condition. (a) South side, (b) Top side, (c) North side, (d) Bottom side**



(a)



(b)

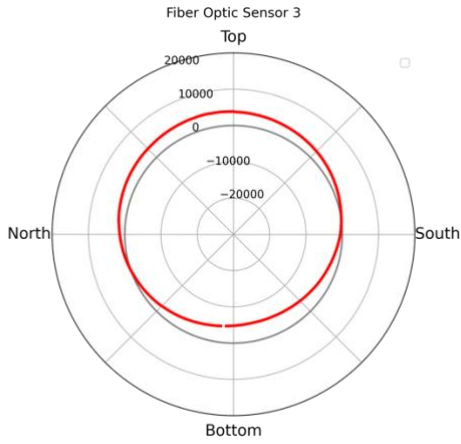
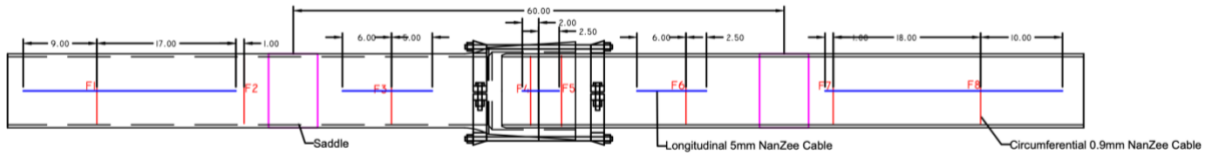


**Figure 4-8 Axial strain development of east pipe of Specimen 2 under 18-degree rotation condition. (a) South side, (b) Top side, (c) North side, (d) Bottom side**

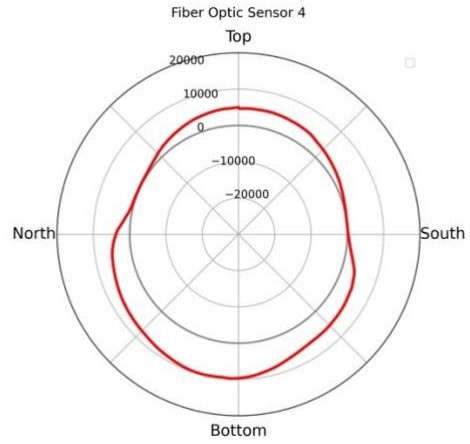
#### 4.2.4 Hoop Strains

The hoop strain results measured from Specimen 1 are plotted in Figure 4-9. The figure shows the results measured by the sensors placed on the bell (F4 and F5) and the sensors that are the closest to the bell on both of the pipes (F3 and F6).

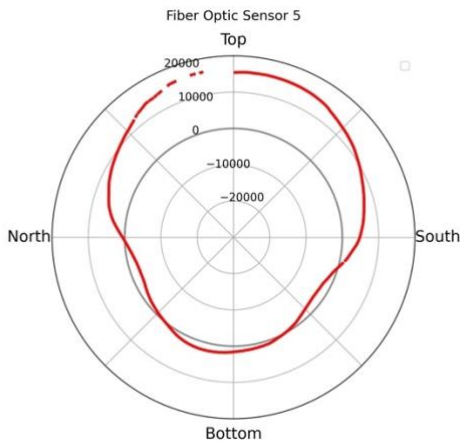
Results of F3 and F6 on the pipes show that the top side (12 o'clock) was expanding, and the bottom side (6 o'clock) was compressing. This is due to Poisson's effect that the strains in the circumferential direction were mainly opposite to those in the longitudinal direction with a smaller magnitude. Tensile hoop strains can be observed at the top side and compressive hoop strains showed at the bottom side with small strains on the other two sides, indicating the pipes were squashing eccentrically during bending. The deformation mechanism of the pipe cross-section is shown in Figure 4-10. The rest of the circumferential sensors placed on the pipes (i.e., F1, F2, F7, and F8) showed similar patterns, as shown in Appendix C. However, the magnitude of the strain decreased as the distance from the sensor to the bell increased.



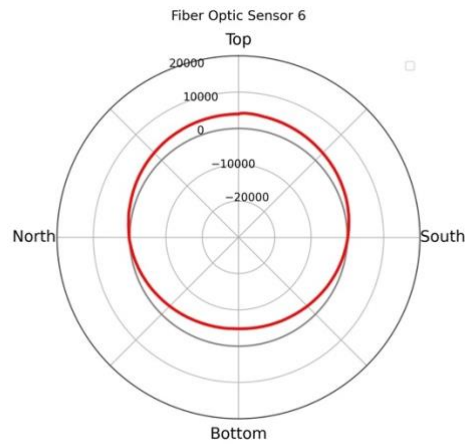
(a)



(b)

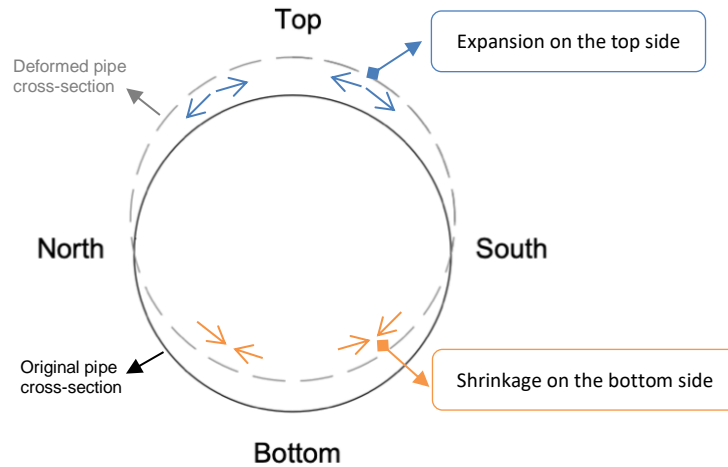


(c)



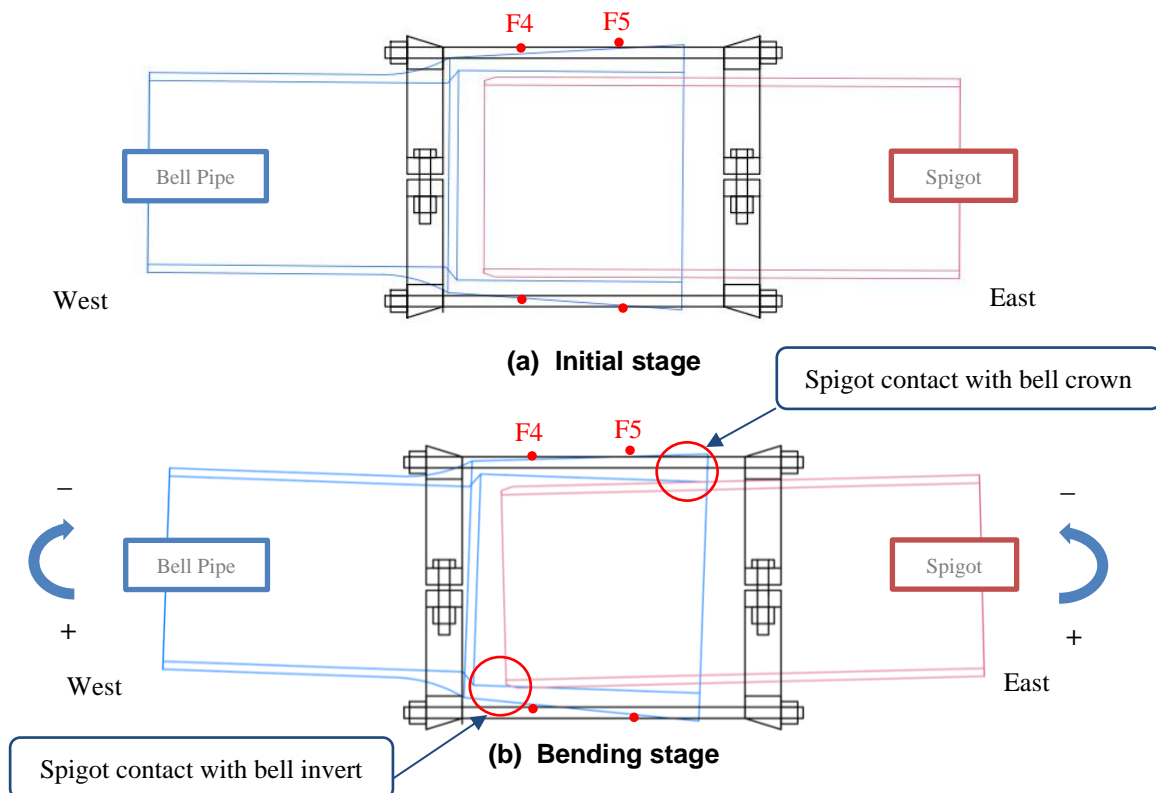
(d)

**Figure 4-9 Strain distribution in the circumferential direction of Specimen 1 under 18-degree rotation condition. (a) sensor on the west pipe (b) sensor on the bell to the west of the center (c) sensor on the bell to the east of the center (d) sensor on the east pipe**



**Figure 4-10 Sketch of pipe cross-section deformation mechanism under bending condition**

Figure 4-11 shows the bell deformation mechanism at the initial stage and under bending conditions. As shown in Figure 4-11(a), the spigot and the bell pipe were not contacted at the initial stage. As the pipe being pushed down, the spigot started to bear against the bell. The two sensors placed on the bell (F4 and F5) showed different patterns. The one to the west side of the center point (F4) showed that the bell was expanding more on the bottom than on the top (see Figure 4-9). This is because the spigot was bearing against the invert of the west side of the bell while being pushed down. On the contrary, for F5, the spigot contacted the crown of the bell face and hence expands the bell on the top resulting in smaller strains at the bottom (see Figure 4-9). The sketch of the mechanism is shown in Figure 4-11(b). The test stopped due to reaching the testing capacity. No severe water leakage or pipe failure was found.

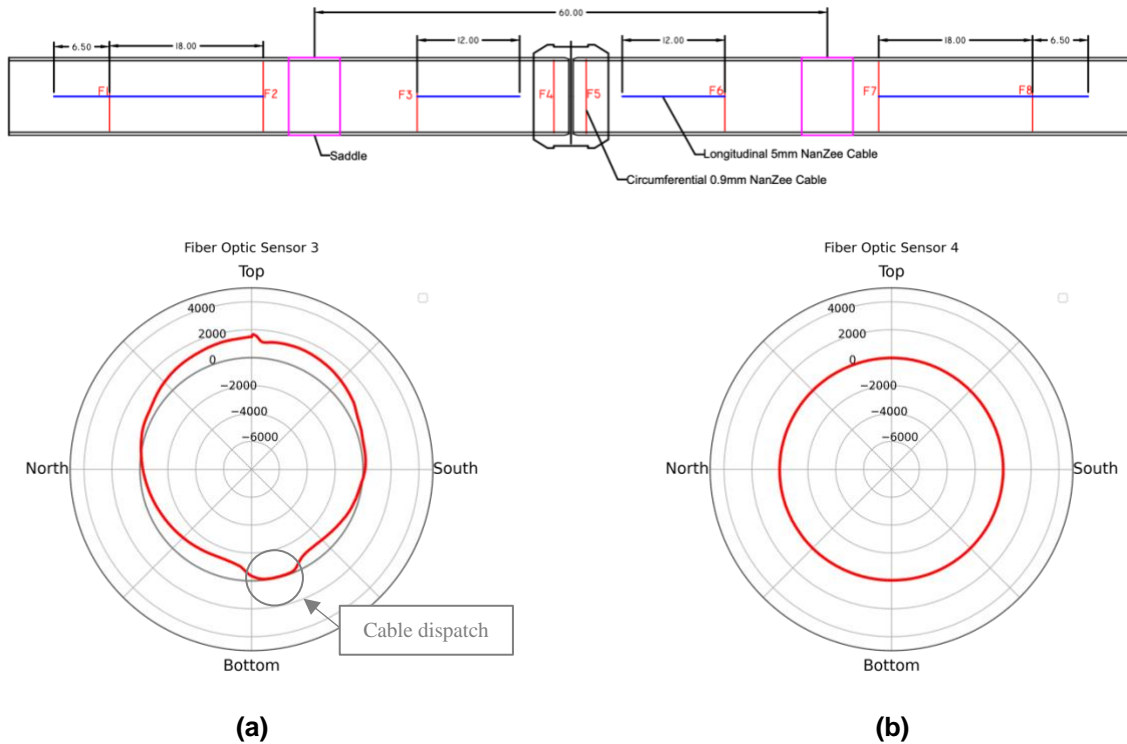


**Figure 4-11 Sketch of EBAA 1900 restraint deformation mechanism**

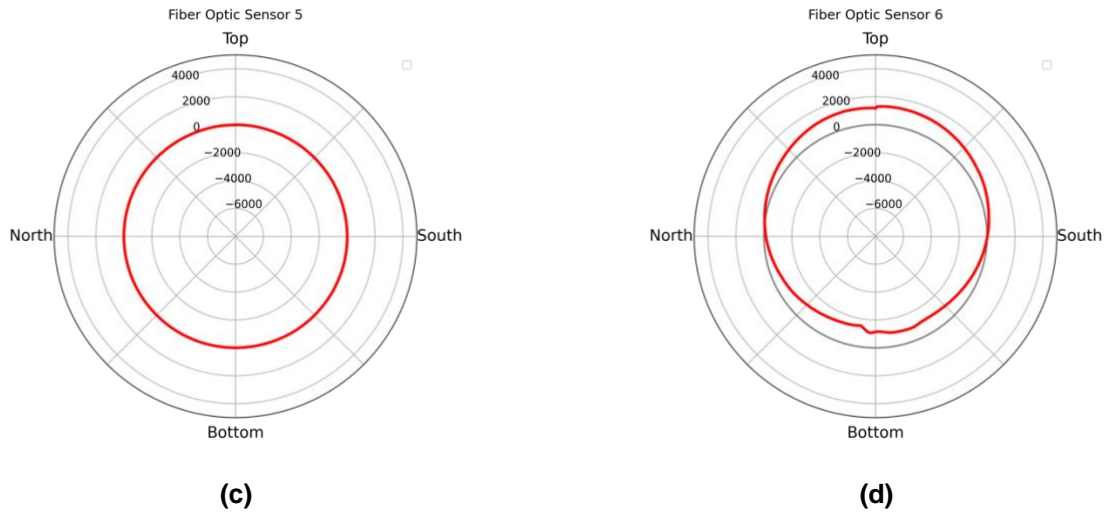
Figure 4-12 shows the hoop strain results in Specimen 2 from Test 2. Two sensors (F3 and F6) were on the pipes closest to the center point, and two were attached to the RCT restraint. Similar to the observations of the pipes in Specimen 1, the pipes were eccentrically squashing, with expansion on the top side (12 o'clock) and compression on the bottom side (6 o'clock). The zero values close to the bottom of F3 are due to cable detachment, shown in Figure 4-12(a). The rest of the sensor results are listed in Appendix C. The results indicated that the pattern on the pipes is similar, but the magnitude varies due to the distance between the sensor and the restraint. The magnitude of the strains is larger when the sensor is closer to the restraint.

In addition, comparing the magnitude of the strain developed on the pipes at a given rotation, the strains are generally smaller in Specimen 2. This is again due to the locking mechanism difference. The EBAA 1900 restraint utilized in Specimen 1 permitted the bell pipe and spigot to make direct contact with each other, leading to greater deformation of the pipes. Conversely, due to the material's stiffness difference, the RCT restraints used for Specimens 2 resulted in significant strain concentration at the top of the pipes near the restraint boundary, while producing smaller deformations elsewhere along the pipes.

The behavior of the restraint is different from the previous one. Since the stiffness of the RCT restraint is much larger, the deformation on the RCT restraint was much smaller than that of the pipes, resulting in smaller strains developed on the restraint. The strains developed on the RCT restraint are close to zero. All the hoop strain results are given in Appendix C.

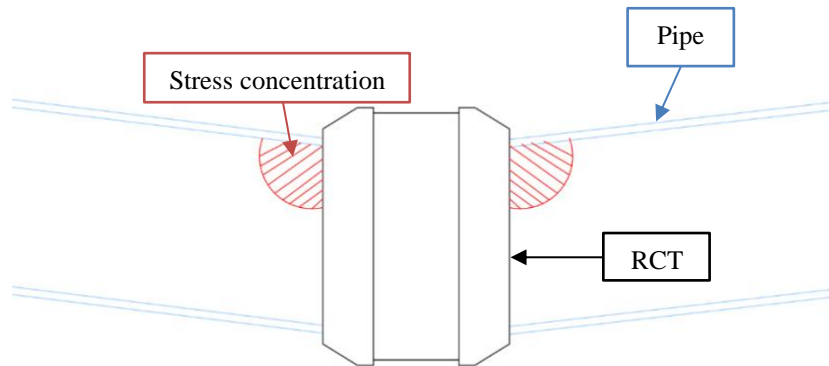






**Figure 4-12 Strain distribution in the circumferential direction of Specimen 2 under 18-degree rotation condition. (a) sensor on the west pipe (b) sensor on the bell to the west of the center (c) sensor on the bell to the east of the center (d) sensor on the east pipe**

The RCT restraint was crafted from ductile iron, which offered superior stiffness. Consequently, while the pipe was being pushed down, it was squashed, but the restraint remained intact. Additionally, due to the large stiffness difference between the restraint and the pipe, a shear force was generated at the boundary, resulting in a large stress concentration at the top of the pipes close to the restraint, where the pipe initially failed. Figure 4-13 illustrates the stress concentration areas. The stress concentrated at those particular locations contributed to a large localized strain, which led to a sudden failure.



**Figure 4-13 Sketch of strain concentration on pipes of Specimen 2**

## 5 Conclusions

This report describes the results of the experiments of an 8-inch AWWA C900 DR14 iPVC pipe with two types of restraints (EBAA 1900 and RCT) under bending force. The experiments were designed to test the pipe until severe damage or water leakage occurred. No severe pipe failure was found on Specimen 1 when the rotation of the pipes reached the capacity of the testing setup (i.e., about 37 degrees of rotation). However, continuous small water leakage was found on Specimen 1 after the rotation reached about 28 degrees. Specimen 2 failed when its rotation reached 34.45 degrees. The pipe broke into two pieces at the boundary of the RCT restraint and the pipe. Generally, for a given rotation, the moment generated in the specimen equipped with EBAA 1900 is greater than that of the specimen with RCT restraint. A shorter length of the RCT restraint and potentially the sliding of the pipes within the restraint might result in a smaller moment.

Fiber optic sensors captured the axial and circumferential strain developments. By viewing the strain distribution, one can observe that the pipes were squashing in the cross-sectional plane. The two restraints resulted in different behaviors in the restrained section. Since the EBAA 1900 restraint allows the pipes to bear against each other, large strains were captured by the circumferential sensors at the bell section (i.e., the restrained area), indicating a large deformation on the bell. However, no severe damage on the bell was found before reaching the testing capacity. On the other hand, due to a larger stiffness, merely no deformation was found on the RCT restraint under the bending force. However, the large stiffness difference at the boundary of the restraint and the pipes contributed to concentrated stress, indicating the weak point is the edge of the two components. Hence, the failure can be sudden. Moreover, due to the difference of the locking mechanism of restraints and greater moment, one would notice that the magnitude of the strains is generally larger on Specimen 1 than Specimen 2 at a given rotation.

## 6 References

PPI Pipe (n.d.). iPVC Water Pipe. <https://ipvcpipe.com/eng/sub/ipvc01.php>

Wu, J., Jiang, H., Su, J., Shi, B., Jiang, Y., & Gu, K. (2015). Application of distributed fiber optic sensing technique in land subsidence monitoring. *Journal of Civil Structural Health Monitoring*, 5(5), 587-597.

# Appendix A: Additional Specimen with RCT Restraint Test Result

An additional trial test was conducted using specimen with the RCT restraint. The experimental setup is similar to the one used for Specimen 2. However, FO sensors were not installed on this specimen. The results and experimental findings are reported in this section. Figure A-1 shows the experimental setup of the additional trial test while the specimen was bent to a large deformation.



**Figure A-1 Experimental setup and large deformation of the additional trial specimen**

During this trial test, the actuator was found not moving exactly toward the desired direction (i.e., point down to the perpendicular axis of the longitudinal direction), but bending was found on the actuator, shown in Figure A-1, which influenced the pushing direction and required larger forces. To ease the situation, a specially designed track was installed to ensure the pushing direction of the actuator for Specimen 2 in Test 2. The specially designed track is shown in Figure A-2.



**Figure A-2 Specially designed track for actuator**

The result of the additional trial test is reported herein. The maximum rotations with corresponding moments of the specimen is 37.14 degrees rotation with 174.6 kip-in moments. As mentioned before, due to the bent actuator, the acquired moment to reach a certain rotation is greater than that of the result from Specimen 2 in Test 2, shown in Figure A-3 (a). Figure A-3 (b) shows the relation between water pressure and the joint rotation of each test. For the additional trial specimen, no obvious pipe failure was found throughout the test until the test reach the limitation of the experiment (about 37-degree rotation). The result of the three tests are reported in Table A-1.

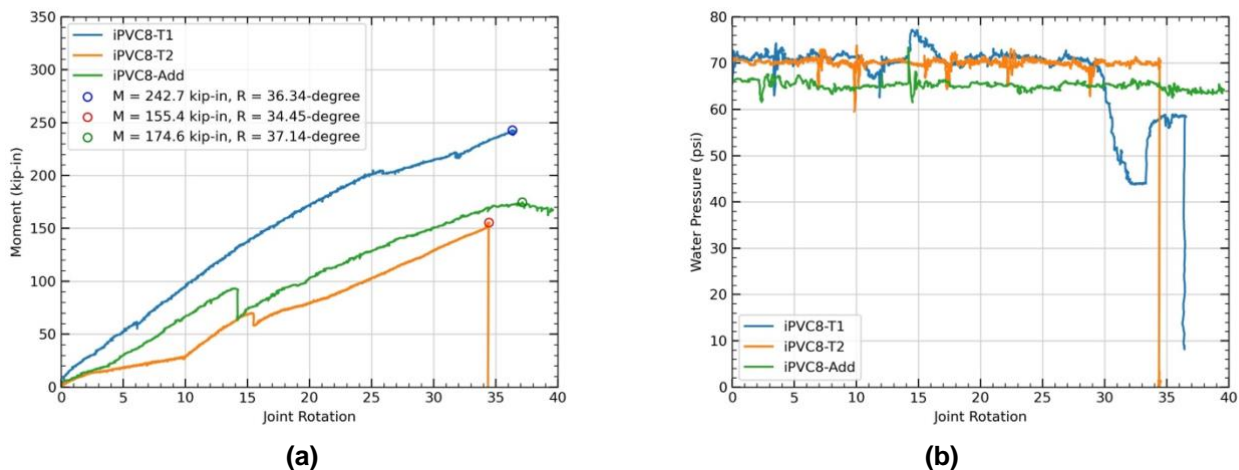


Figure A-3 Moment, rotation, and water pressure of the tests. (a) Joint rotation versus moment (b) Joint rotation versus water pressure

Table A-1 Summary of the tests

	Max. Moment (kip-in)	Max. Total Rotation (degree)	Pipe Failure	Restraint Type
<b>Specimen 1</b>	242.7	36.34	No	EBAA1900
<b>Specimen 2</b>	155.4	34.45	Yes	RCT
<b>Specimen Add</b>	174.6	37.14	No	RCT

# Appendix B: Distributed Fiber Optic Sensing

Using the physical properties of light, fiber-optic sensing can detect changes in temperature, strain, and other parameters when light travels along a fiber, which uses fiber-optic cables as sensors and can measure over long distances at 100 to 1000s of points on a single cable or multiplexed cables depending on the analyzer used. Compared to the other sensing technologies, fiber-optic sensing has distinct advantages such as small size, light weight, and strong resistance to corrosion and water. Distributed fiber optic sensing consists of two main components, an analyzer, and fiber-optic cables. LUNA ODiSI 6000 series integrator was used as the analyzer, and NanZee Sensing Technology Co manufactured the fiber-optic cables in the experiments.

## LUNA Interrogator




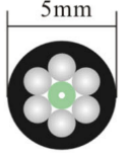
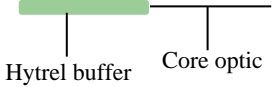
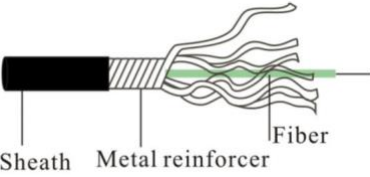
**Figure B-1. LUNA ODiSI 6000 Series optical distributed sensor interrogator (LUNA, 2022)**

LUNA ODiSI 6104 is an optical distributed sensor interrogator that can provide thousands of strain or temperature measurements per meter of a single high-definition fiber sensor. High-Definition H.D.D) Sensors - Strain & Temperature (HD-SC) temperature sensors utilize an advanced interrogation mode of the ODiSI to increase the accuracy of measurements when the sensors are subjected to strain, such as in embedded and surface-mount installations. It can achieve a sensor gauge pitch (the distance between two measurement points) as small as 0.65 mm, a sensor length of up to 50 m, and a measurement rate of up to 250 Hz with an accuracy of less than  $\pm 1$  microstrain.

## Fiber-optic Cable

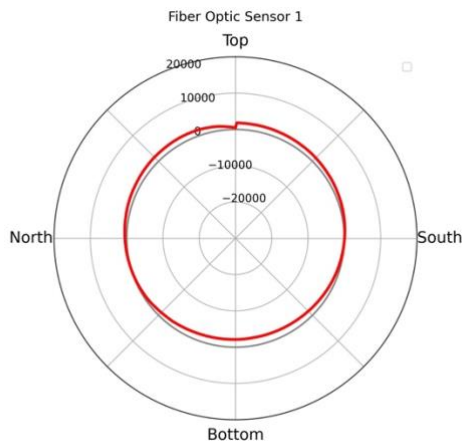
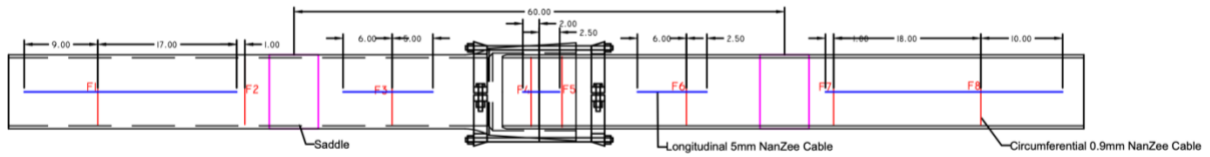
Two types of fiber optic cables manufactured by NanZee Sensing Technology Co. were used; (a) 5 mm diameter armored cable (NanZee 5mm) and (b) 0.9 mm diameter cable (NanZee 0.9mm). Table B-1 lists the information on the cables. The difference between the two cables is the thickness and material of the coating. NanZee, a 5mm cable, provides a sheath layer and steel reinforcement, resulting in better protection to the optical core; hence, it can be used for the actual field application. The coating of NanZee 0.9mm cable is thinner than NanZee 5mm cable. NanZee 0.9mm cable has less protection, but a more sensitive strain response is achieved.

**Table B-1 Schematic illustration of the selected strain sensor cable (Wu et al., 2015)**

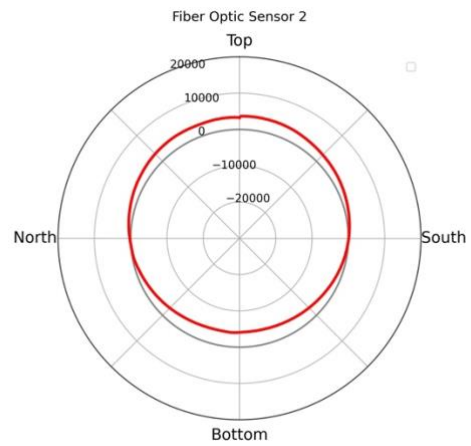
Brand	NanZee Sensing Technology Co.	
Model	NZS-DSS-C07	NZS-DSS-C02
Cross section		
Side view		

# Appendix C: Fiber Optic Sensors Result

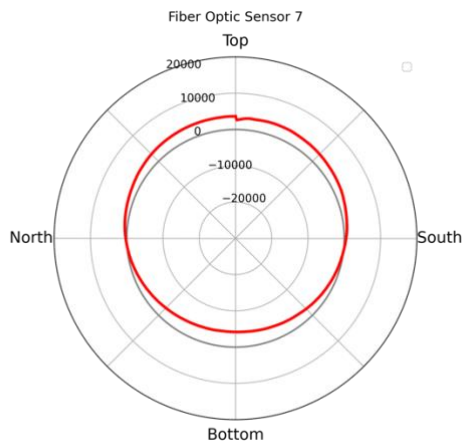
The hoop strain results from the distributed fiber optic sensors are demonstrated herein.



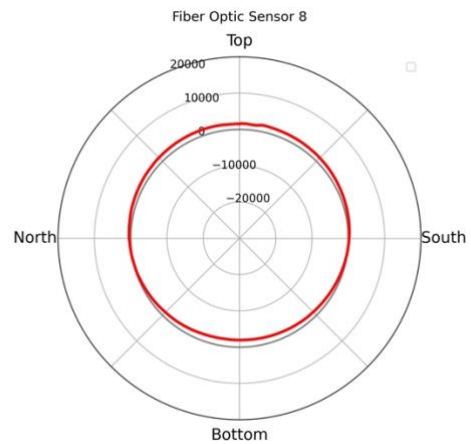
(a)



(b)



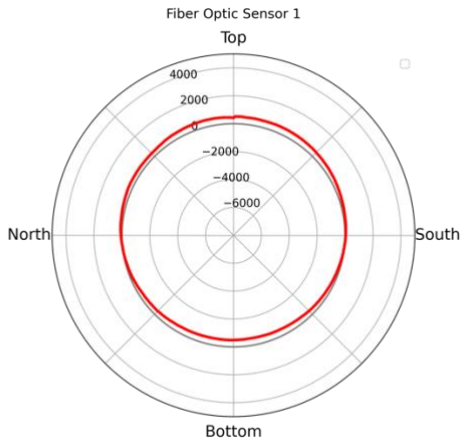
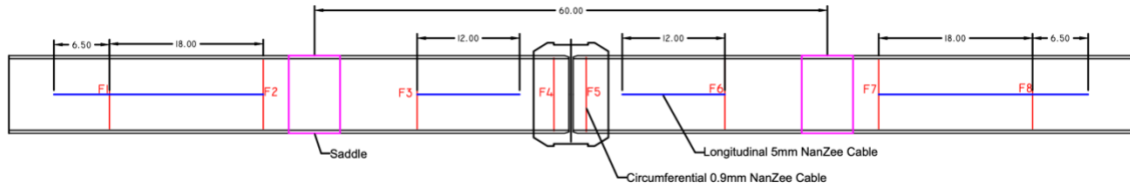
(c)



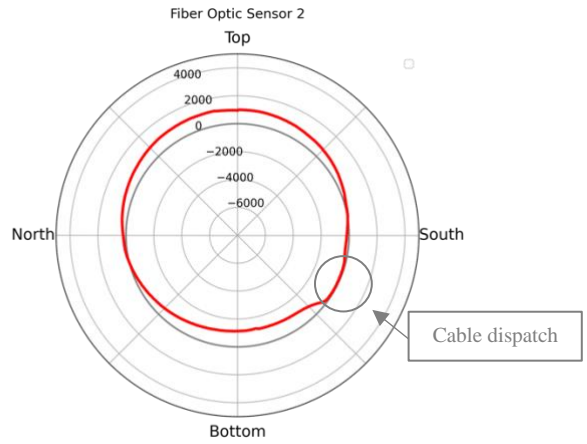
(d)

Figure C-1 Strain distribution in the circumferential direction of Specimen 1 under 18-degree rotation condition. (a)(b) sensors on the west pipe (c)(d) sensors on the east pipe

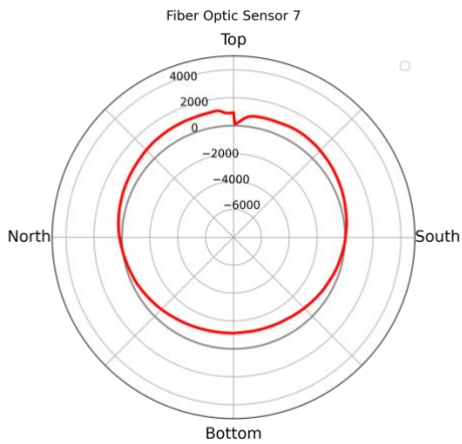




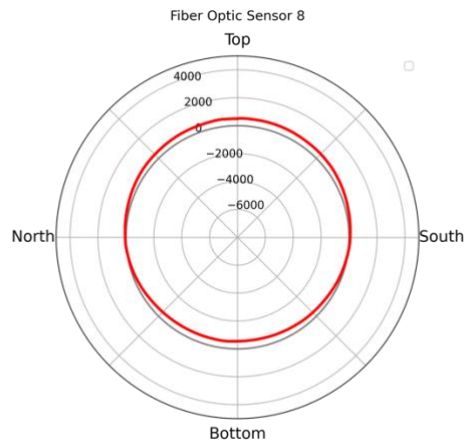
(a)



(b)



(c)



(d)

**Figure C-2 Strain distribution in the circumferential direction of Specimen 2 under 18-degree rotation condition. (a)(b) sensors on the west pipe (c)(d) sensors on the east pipe**